# Automated assessment of tDCS electrode placement accuracy based on structural MRI

Sina Straub[1,2], Raphaela Schöpfer[1,2,3], Sarah Godehardt[1,2,3], Florian Wüthrich[1,2], Jessica Peter[1,2]

[1]University Hospital of Old Age Psychiatry and Psychotherapy, University of Bern, Bern, Switzerland

[2]Translational Imaging Centre, Swiss Institute for Translational and Entrepreneurial Medicine, Bern, Switzerland

[3]Graduate School for Health Sciences, Faculty of Medicine, University of Bern, Bern, Switzerland

Corresponding author:

Dr. rer. nat. Sina Straub

University of Bern

Department of Old Age Psychiatry and Psychotherapy

Bolligenstrasse 111

CH-3000 Bern 60

Keywords: tDCS, tDCS-MRI, electrode placement verification, neuromodulation

**Abstract**

Purpose: Accurate electrode placement is essential for studies using transcranial direct current stimulation (tDCS) since it determines whether – and to which extent - the intended brain region was modulated. Precise electrode placement also reduces between-subject variability. Using in-scanner tDCS, accuracy and precision of electrode placement can be determined. Previous studies manually segmented electrode positions from structural MRI, a process that is time-consuming and prone to error. We therefore developed an algorithm that automatedly extracts electrode coordinates from structural MRI.

Methods: We applied this algorithm to 49 datasets acquired at different field strengths (3 T and 7 T), with two image resolutions and electrode montages (bifrontal or ring-shaped) targeting the dorsolateral prefrontal cortex. We validated its accuracy by comparing the automatedly extracted coordinates with manual annotations from two independent readers. We then used the actual and intended electrode coordinates to simulate how electrode placement deviations influenced the resulting electric field.

Results: For all setups and scanners, the median localization error of the algorithm was 2.3 mm. It was within 1 mm of the variability between human readers (2.7 mm), indicating human-level reliability. Large deviations (> 20 mm) from intended positions led to substantial changes in the electric field - up to 35% for the ring-shaped montage -highlighting the need for placement verification in tDCS studies.

Conclusion: The proposed algorithm obviates the need for manual electrode segmentation and allows an objective evaluation of electrode placement accuracy and precision for in-scanner tDCS. It may be used to relate electrode position errors to stimulation effects, thereby supporting reproducible tDCS research.

## Introduction

Transcranial direct current stimulation (tDCS) is a non-invasive brain stimulation method that modulates the excitability of targeted brain regions by applying a weak constant current (typically 1-2 mA) to the scalp[1–3]. It has been used to enhance or inhibit a wide range of cognitive functions, such as working memory[4,5], attention[6], or motor learning[1]. In addition, it is being investigated as an adjunct treatment for major depressive disorder[7,8] or for promoting recovery after stroke[3,9,10]. tDCS can be applied using conventional large-pad montages, usually with two electrodes, or multi-electrode high-definition configurations[11] with small electrodes (most commonly in a 4x1 ring-shape), which enhance current focality and spatial accuracy[6]. For both setups, electrode placement is commonly guided by cranial landmarks[12–15], although some studies used neuronavigation-based approaches[12,16], which require multiple MRI scans. Deviations in electrode positioning alter current distribution patterns[17–20] and the extent of cortical modulation, likely contributing to variability in stimulation outcomes[21,22] and to reduced reproducibility across studies. This may be particularly so for high-definition tDCS due to its higher focality. For conventional montages with large pad electrodes, simulations indicated that small deviations from intended positions (i.e., 10 – 15 mm on an adult head) significantly altered the spatial current flow profile[20]. In addition, correlations with intended electrical field distributions indicated a substantial reduction in the similarity between delivered and intended stimulation patterns for larger placement errors (i.e., r = 0.8 for deviations of 10 mm, r = 0.6 for deviations of 20 mm). When using in-scanner tDCS, structural MRI data can be used to extract actual electrode positions and consequently to evaluate placement accuracy and precision. Simulation tools such as SimNIBS[23], ROAST[24] or Shamo[25] then allow an examination of how much those deviations influenced the electric field. For conventional tDCS, one study that determined actual electrode positions from MRI data reported no substantial reduction in the electric field of the target region despite electrode misplacements[17]. For high-definition tDCS, a displacement of 7 mm led to less than a 5% reduction in the target-region electric field[12]. Deviations of 10–20 mm, however, resulted in an approximate 27% reduction[17]. Deviations of 20 mm led to a ~30% reduction of the electric field in the target region and to a markedly

lower correlation with the intended field (r = 0.58)[12]. Hence, there is need for accurate and precise electrode placement when using tDCS. Quantifying deviations from intended positions may help identify sources of error and reduce variability across studies. In addition, the actual electrode position can be related to the physiological, neuroanatomical, and behavioural effects of stimulation. So far, electrode positions were extracted manually from structural MRI data[17,18,26,27], a process that is time-consuming and may be prone to error or bias. We therefore developed an automated algorithm to extract electrode positions (i.e., coordinates) from structural MRI data. We used this algorithm to extract electrode positions from MRI data with two different image resolutions acquired at two different scanners (3 T and 7 T) and two different electrode montages (bifrontal or ring-shaped). We then validated the algorithm by comparing extracted electrode positions with manual annotations by two independent readers. All montages targeted the dorsolateral prefrontal cortex (dlPFC). Although the main objective of this study was to develop and validate an algorithm to extract electrodes automatedly, we also assessed how deviations from intended positions influenced the electric field in our target region. To do so, we performed individualized electric field simulations for intended and actual electrode positions.

## Material and methods

### *Participants*

We included data of n = 50 participants of two randomised, double-blind, and sham-controlled clinical trials. All studies targeted the left dlPFC. Participants (mean age 28.6 ±14.0 years, age range 20-73 years, 30 female) were either healthy or had a diagnosis of major depressive disorder as confirmed by clinical interview before study participation. All participants had to be fluent in German, right-handed, non-smokers, non-alcohol or -drug abusers, with normal or corrected-to-normal vision, and no history of neurological or psychiatric disorders (except for patients with depression). All data were collected at the University of Bern. All participants provided written informed consent before the study. The cantonal

Ethics Committee approved the studies (2017-01664, 2024-01010) which were done in accordance with the Declaration of Helsinki and its amendments.

*MRI data acquisition and processing*

After study inclusion, participants were randomly assigned to receive either sham or real high-definition tDCS (1 mA for 20 min; Soterix Medical Inc., Woodbridge, NJ, USA), while undergoing 3 T (MAGNETOM Prisma, Siemens Healthineers, Erlangen, Germany) or 7 T MRI (MAGNETOM Terra, Siemens Healthineers, Erlangen, Germany). We used a 1Tx-32Rx (Nova Medical Inc., Wilmington, MA, USA) head coil at 7 T or a 64Rx head coil at 3 T. Before starting the stimulation, we acquired structural MRI data using a compressed-sensing accelerated MP2RAGE sequence with sagittal slice orientation (Table 1). We then used the structural MRI data to create head meshes and tissue segmentations by applying SimNIBS' (Version 4.5) CHARM algorithm[28,29].

**Table 1.** MP2RAGE sequence parameters

| | **resolution in mm$^3$** | **matrix size** | **repetition time in ms** | **echo time in ms** | **inversion time in ms** | **flip angle in °** | **bandwidth in Hz/pixel** | **acquisition time in min:sec** |
|---|---|---|---|---|---|---|---|---|
| **7T** | 0.63×0.63×0.63 | 384×384×256 | 6000 | 2.06 | 800/ 2700 | 4/ 5 | 240 | 7:40 |
| **3T** | 1.0×1.0×1.0 | 256×256×176 | 5800 | 2.9 | 800/ 2200 | 5/5 | 240 | 4:14 |

*Abbreviations*: mm = millimetre, ms = milliseconds, Hz = Hertz, min = minutes, sec = seconds, T = Tesla.

*Transcranial direct current stimulation*

We used two different electrode montages and placed electrodes according to the 10-20 EEG system[30]. For healthy participants, we placed the centre electrode (i.e., the anode) at position F3 and the four adjoining electrodes at F1, FC3, F5 and AF3, respectively. For patients with depression, we placed the anode at F3 and the cathode at F4. We used silver-chloride ring electrodes or rectangular carbon rubber electrodes with corresponding electrode holders, EEG caps (all from Soterix Medical Inc.), and paste (Abralyt, Easycap GmbH, Wörthersee-Etterschlag, Germany) as well as MR-visible gel (Signa gel, Parker

Laboratories Inc., Fairfield, NJ, USA). We quantified the amount of MRI-visible added gel in all participants.

**Figure 1:** Flowchart of the algorithm (A) and graphical illustration of the seven steps of the algorithm including electrode segmentation (B-D) and coordinate extraction (E). (C) An initial mask (beige) is shown that includes all voxels above a certain slice threshold other than those segmented by CHARM's tissue segmentation. Spatial priors (Prior 1 for the two-electrode montage, Prior 2 for the five-electrode montage) were used to refine this initial mask. White arrows indicate voxels that were incorrectly segmented during this step. (D) initial electrode mask (red). (E) connected components to which the electrode mask was split and the extracted centroids (yellow arrows). At the end, a prompt opens that shows the actual (blue circles) and intended (magenta circles) electrode coordinates.

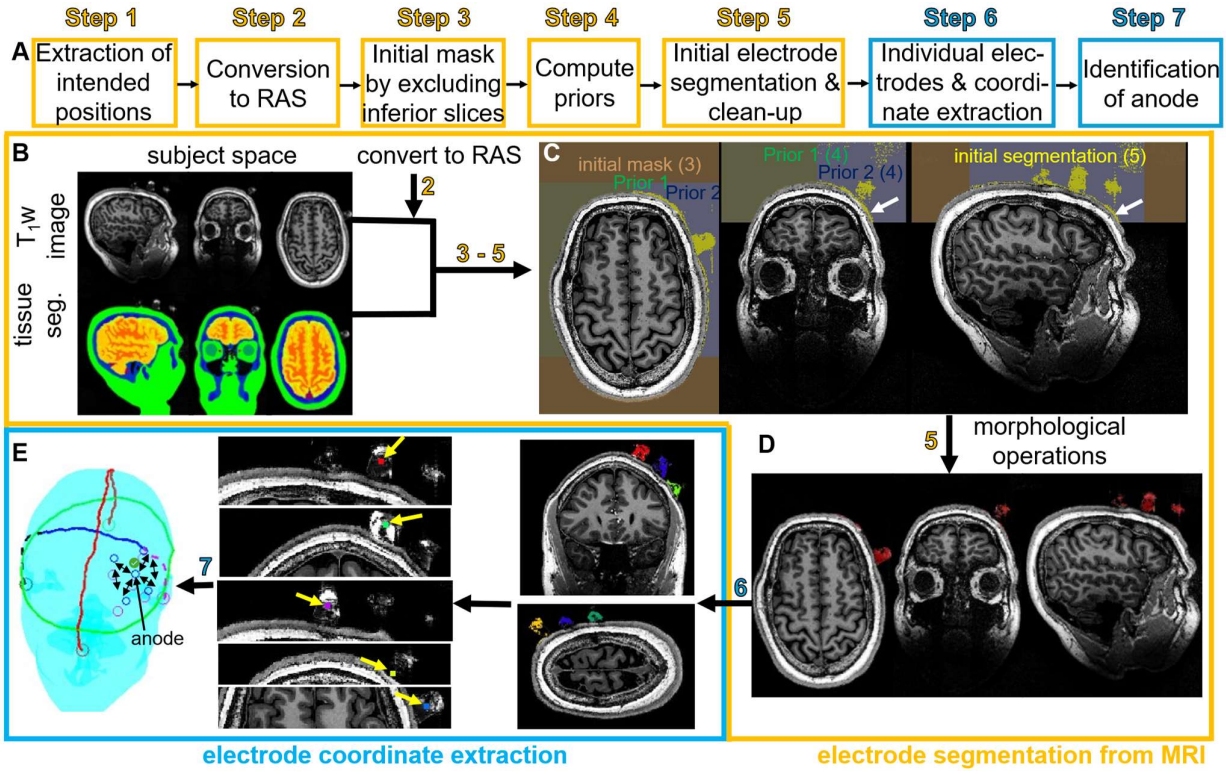


*Algorithm design*

We developed an algorithm implemented in Matlab (Version R2024b, MathWorks, Inc., Natick, MA, USA) which uses the CHARM syntax for folder names and structures (e.g., structural $T_1$-weighted data and the tissue segmentation need to be stored as zipped NIfTI files "T1.nii.gz" and "final_tissues.nii.gz"). The algorithm is freely available on github: GitHub - SinaStraub/tDCS_automated_electrode_location_from_MRI). The algorithm consists of electrode segmentation from structural MRI data (Step 1-5, Figure 1A-D) and coordinate extraction from this

segmentation (Step 6-7; Figure 1A, E). Input parameters for our proposed algorithm are listed and described in Table 2.

**Table 2**. Input parameter for the proposed algorithm.

| Parameter | Description |
|---|---|
| fullpath | Path to the location of the participant directory. This directory needs to contain structural $T_1$-weighted MRI data (named "T1.nii.gz"), the head mesh (named "ParticipantID.msh"), and tissue segmentation (named "final_tissues.nii.gz"). |
| subdir | m2m_participantID |
| numElec | Number of electrodes in the used montage. |
| elec_list | List of intended electrode positions according to 10-10 EEG system. |
| smallblobsize | Parameter to remove artificially segmented voxels during morphological operations. Recommended: 30. |
| cutoffpositionz | Slice cutoff position in head-feet direction to exclude inferior slices on which no electrodes can be expected. |
| thres_factor (optional) | Multiplied by the mean normalized $T_1$-weighted signal intensity within the voxels not belonging to the tissue segmentation to obtain the threshold which is used to compute the initial electrode segmentation in Step 5. Default: 2. |

Step 1: The head mesh is used to extract coordinates of intended electrode positions based on the 10-10 EEG system.

Step 2: Structural MRI data and tissue segmentations are converted to the Right-Anterior-Superior (RAS) coordinate system (Figure 1B) using ROAST's Matlab function `convertToRAS`. The voxel size of the data is extracted from NIfTI headers.

Step 3: An initial mask is computed by first excluding all voxels below a certain slice position where no electrodes can be expected. This slice position is an input parameter for the algorithm.

Everywhere else, where the CHARM tissue segmentation is zero, this initial mask is set to one (Figure 1C).

Step 4: Based on tissue segmentation, voxel size, and electrode configuration, a spatial prior is created to exclude head surface areas from the mask, where no electrodes are located (Figure 1C): For the electrode montage with two electrodes, the prior excludes coronal slices from front and back of the head using the brain boundary which is extracted from CHARM's tissue mask. For the montage with five electrodes, sagittal slices on the right of the head are excluded in addition. This step uses the function `electrode_loc_prior`.

Step 5: After normalizing the $T_1$-weighted image to a 0–1 intensity range, the mean voxel intensity within the resulting mask from the previous step is computed. An initial electrode segmentation is obtained by retaining only voxels with normalized $T_1$-weighted values exceeding this mean times a thresholding factor. This factor is provided to the algorithm as an input parameter (Table 2). The resulting initial electrode segmentation is then eroded and morphologically opened (Figure 1D).

Step 6: Individual electrode coordinates are extracted from the resulting electrode mask by identifying connected components using the Matlab function `bwconncomp` (Figure 1E): The connected components are filtered by size and elongation. Large connected components are split and again filtered by elongation. The connected components that survived filtering are sorted by size, small clusters are deleted, and large clusters are split using `kmeans` clustering[31] until the number of clusters equals the number of electrodes. From the final connected components, centroids are extracted and used as actual electrode coordinates (Figure 1E).

Step 7: The anode is automatedly identified by comparing voxel coordinates with the function `get_anode`. This is straightforward for the bifrontal montage but can become ambiguous for the five-electrode montage. For this montage, the algorithm sorts the x- and y-coordinates of all electrodes and identifies the anode as the electrode whose x and y values both fall in the middle of those sorted lists (Figure 1E). If median x and median y come from different electrodes, an image

with all electrode coordinates appears, and the user is prompted to specify the position of the anode manually.

After completing Step 1-7, the algorithm writes extracted subject space coordinates in a text file in the participant folder, with anode (A1) followed by cathodes (C2, ..., Cn). In addition, it creates a NIfTI file containing the centroids for each electrode ("landmarks.nii") that allow the user to verify extracted positions on MRI data. Two NIfTI files containing the prior from Step 4 ("h1.nii" and "h2.nii") are stored to help visualise which skull regions were used for electrode segmentation and to facilitate a quick adjustment of prior computation (Step 4) for other electrode setups in the future. Then, the algorithm forwards actual and intended electrode positions to SimNIBS and runs electric field simulations using the SimNIBS function `run_simnibs` in Matlab.

*Algorithm implementation and evaluation*

We used 270 as slice cutoff for 7 T data and 190 for 3 T data. We used 30 as the parameter 'smallblobsize' and the default thresholding factor of two. In addition, we tested the algorithm without Step 4 (i.e., without the use of the spatial prior).

To evaluate the accuracy of the algorithm, two independent readers (RS, FW; with three or eight years of neuroimaging experience) manually determined electrode locations from MRI data by placing electrode coordinates in the middle of the electrode 'blob' using fsleyes (https://git.fmrib.ox.ac.uk/fsl/fsleyes/fsleyes/). That blob corresponded to MR-visible high-intensity regions from gel surrounding the electrode. We did not ask readers to differentiate between anode and cathodes as this was deemed too difficult and time-consuming. Instead, we assigned anode and cathodes automatedly in Matlab by matching each reader coordinate to the closest algorithm-derived coordinate. The intended electrode positions were assigned by the same matching scheme. Then, reader coordinates were averaged to use the mean as a reference, and the Euclidean distance to the automatedly extracted coordinates was computed. In addition, we computed the Euclidean distance

between intended and actual electrode position. We report differences between Euclidean distances as median and interquartile range (IQR) and visualise their distribution using violin plots created with grpandplot[32]. We used one-sided Wilcoxon signed-rank test to examine whether the distance between algorithm- and reader-derived coordinates was smaller than the distance between readers. We considered $p < 0.05$ statistically significant. To examine the relationship between inter-reader distance and algorithm–reader distance, we created a scatter plot. For visualisation, we converted anode coordinates to MNI space using SimNIBS' `subject2mni_coords` function in Matlab.

*Electric field simulations*

We performed electric (E) field simulations using SimNIBS[23] on intended and actual electrode positions. As input for SimNIBS, we entered electrode specifications (i.e., ring electrodes with outer diameter of 12 mm, inner diameter of 6 mm and a thickness of 3 mm), the use of 1 mA for stimulation, and used otherwise default parameters. Our code, as provided on github (https://github.com/SinaStraub/tDCS_automated_electrode_location_from_MRI/tree/main) includes a function `simNibs_template` for electric field simulations which partly reproduces code examples provided within SimNIBS. To quantify key features of the electric field magnitude distributions, we extracted the peak electric field coordinates and the 99.9$^{th}$ percentile of the field magnitude from the subject-space electric field maps. Electric field maps were computed in subject space and in fsaverage space[33,34]. Using the latter, we generated group-level electric field maps for the electric field magnitude by averaging subject-level maps voxel-wise (mean) using SimNIBS' Matlab tools. For the electric field magnitude, we computed group-level standard deviations, too. To assess the E-field in our target region (i.e., dlPFC), we used the labels p9-46v, 46, and 9-46d from the HCP_MMP1.0 parcellation in fsaverage space[33,34]. These regions are located within the dlPFC and roughly correspond to Brodmann areas 9 and 46. We also considered other labels in the vicinity of the dlPFC (a9-46v, IFSa, 8Ad, 8Av, 8BL, 8C, s6-8, i6-8, 9a, 9p) that correspond to Brodman areas 8, 9, 46 or to transitions zones between them (except for IFSa, the anterior part of the inferior frontal sulcus). For subject-level region-of-interest (ROI)

comparisons, we visualised distributions using violin plots created with grpandplot[32] and report median E-field magnitudes with IQRs. We then examined whether the simulated electric fields differed between actual and intended electrode position using two-sided Wilcoxon signed-rank tests, with $p < 0.05$ considered statistically significant. For visualization, we converted electric field peak coordinates to MNI space using `subject2mni_coords`.

**Figure 2:** The distance between electrode locations segmented by the algorithm and the mean locations of the two readers for anodes and cathodes. In addition, the difference between the locations segmented by the algorithm and the intended locations are shown as well as the distance between the readers. Data are grouped by scanner, electrode configuration (3 T – blue; 7 T two electrodes – orange; 7 T five electrodes – yellow). Data for anodes and cathodes are shown separately.

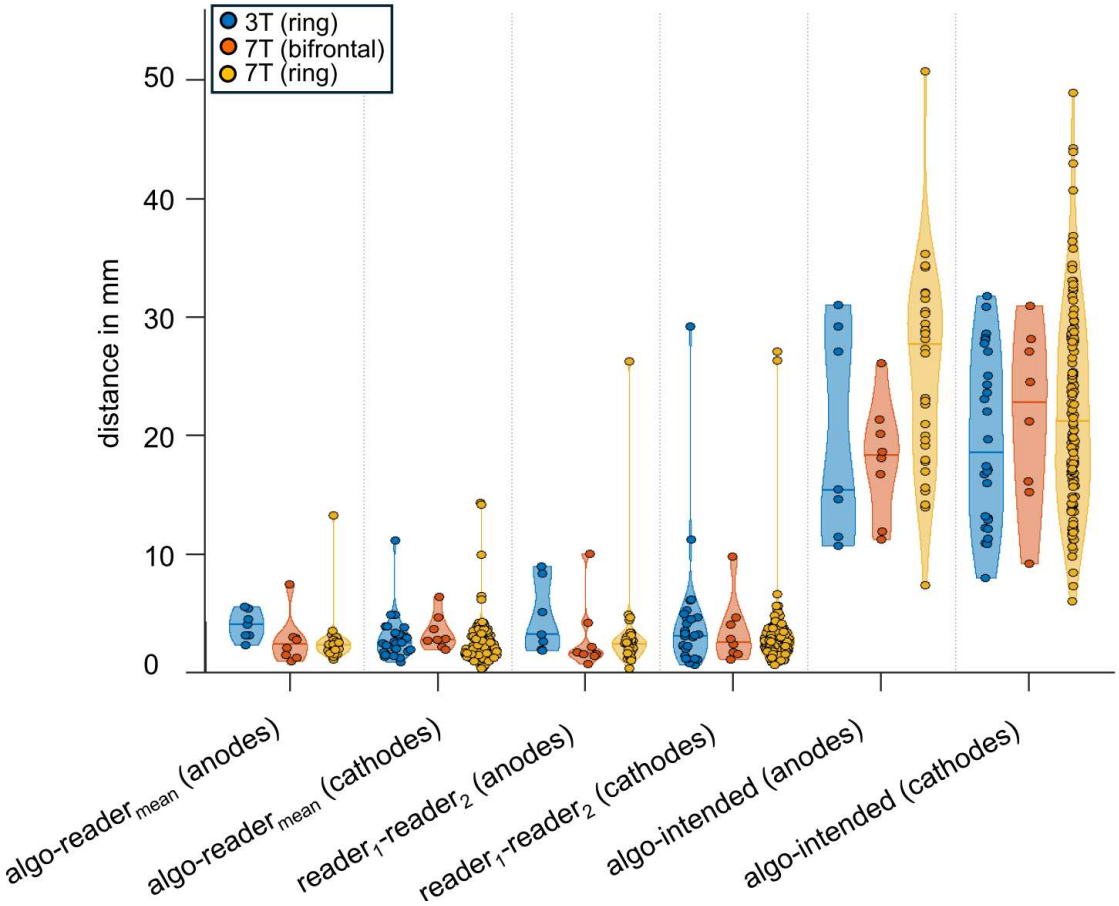


**Results**

We had to exclude one participant due to movement artifacts and therefore evaluated data of n = 49 participants. We used an average of 8.3 g gel for 7 T MRI data or 4.9 g for 3 T MRI data. The readers

reported difficulties in finding electrodes for the 3 T data which have a lower spatial resolution and for which less MR-visible gel was used.

**Table 3.** Euclidean distances in millimetre. P-values represent results of Wilcoxon signed-rank tests (one-sided). Significant values are shown in bold.

| | **algorithm-reader$_{mean}$** | | **reader$_1$-reader$_2$** | | |
|---|---|---|---|---|---|
| **field strength and set-up** | median | IQR | median | IQR | *p*-value |
| 7 T, bifrontal, anode | 2.4 | 1.6 | 1.7 | 1.7 | 0.473 |
| 7 T, bifrontal, cathodes | 2.8 | 1.7 | 2.6 | 2.8 | 0.422 |
| 7 T, ring-shaped, anode | 2.4 | 0.8 | 2.5 | 1.3 | 0.242 |
| 7 T, ring-shaped, cathodes | 2.1 | 1.6 | 2.7 | 1.6 | **< 0.001** |
| 3 T, ring-shaped, anode | 4.1 | 2.1 | 3.3 | 5.5 | 0.406 |
| 3 T, ring-shaped, cathodes | 2.5 | 1.6 | 2.7 | 2.9 | 0.059 |

*Abbreviation*: IQR = interquartile range.

*Performance of the proposed algorithm*

When using the prior (i.e., Step 4), the algorithm prompted to receive coordinates of the anode in six participants. When omitting the prior, this happened in 12 out of the 49 participants. For further evaluation, we used the results of the algorithm with the prior.

The median distance between the algorithm-derived and reader-derived coordinates (2.3 mm, IQR = 1.5 mm) was similar to the median distance between the two readers (2.7 mm, IQR = 1.7 mm). For all setups and scanners, the algorithm disagreed with human readers slightly less than both readers disagreed (below 1 mm; Table 3). The algorithm detected the actual electrode position slightly, but, in part, significantly more accurately than both readers (Table 3). For all coordinates, distances between readers ranged from 0.4 to 29.2 mm, while distances between the reader average and algorithm ranged from 0.4 to 14.3 mm (see Figure 2 for an illustration of all distances). These results indicate that the algorithm determined actual electrode positions with high accuracy. To better understand whether any

disagreement between readers and algorithm was due to an algorithm error or due to variability within readers, we compared algorithm-reader distances and distances between both readers. Figure 3 illustrates that larger distances between readers and algorithm occurred when the two readers did not align and not due to an algorithm error.

**Figure 3:** Scatter plot showing the distances between the two readers and the distances between the readers and the algorithm. The black line indicates the identity line. Data is group by scanner and electrode configuration (3 T – blue; 7 T two electrodes – orange; 7 T five electrodes – yellow) and by cathodes (stars) and anodes (dots).

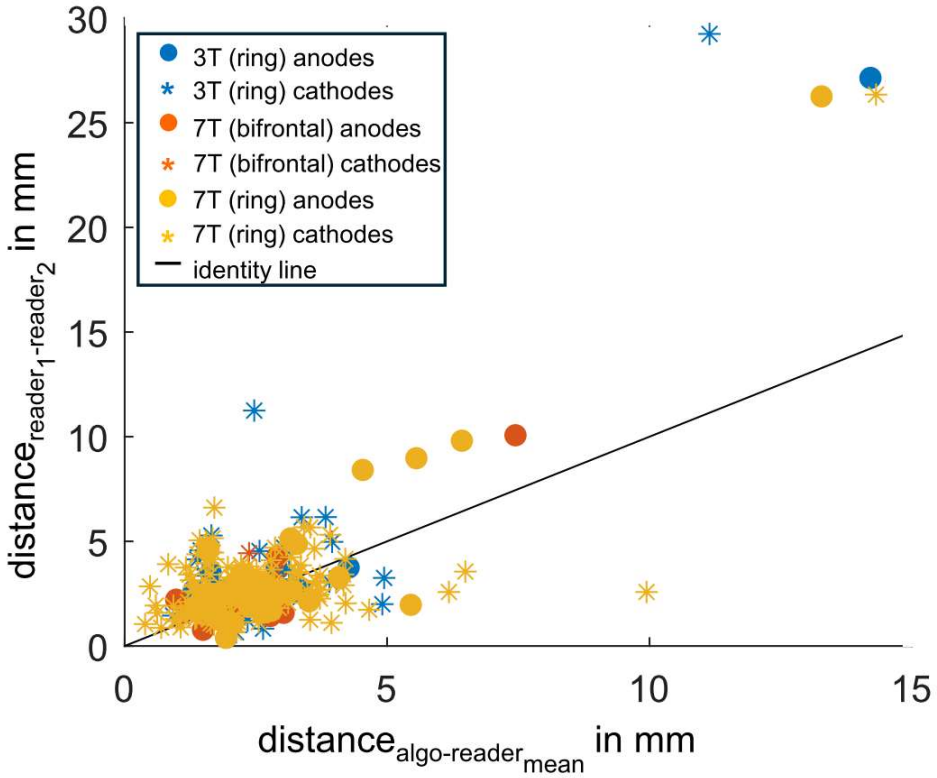


*Assessment of E-field variations induced by deviations from intended electrode positions*

Distances between intended and actual electrode positions ranged from 6.0 mm to 50.8 mm (median = 21.6 mm, IQR = 12.3 mm; see Figure 2, and 4a for anode locations). Electrode placement deviations shifted the peak electric field locations. While many peak field coordinates based on intended electrode positions (50 % bifrontal, 95 % ring) fell within the dlPFC, most peak locations (71 % for both setups) based on actual electrode positions (Figure 4a) were located outside the dlPFC (Figure 4b). When deviations from the intended anode location were small (< 15 mm), the 99.9th percentile of the

electric field magnitude was only minimally affected, changing by 5 % or 8 % (Figure 5, Columns 1 and 3; light-blue values). In contrast, when deviations were larger (> 20 mm), the 99.9th-percentile of the electric field magnitude changed substantially, that is, by 35 % for the ring-shaped montage or 9 % for the bifrontal montage (Figure 5, Columns 2 and 4; light-blue values). In the ROI (i.e., the dlPFC), changes to the electric field magnitude were smaller and ranged from 0 to 17 % (Figure 5, values in purple).

**Figure 4:** Intended (blue) and actual (pink, green, yellow) anode locations (A) as well as resulting peak electric field coordinates (intended yellow, white, blue; actual green, black, pink) (B) overlaid on fsaverage cortical surface. Colours indicate the dorsolateral prefrontal cortex (dlPFC), the frontal eye field / superior frontal cortex (FEF/ SFC), and the medial prefrontal cortex (mPFC). Labels were used from the HCP_MMP1.0 atlas.

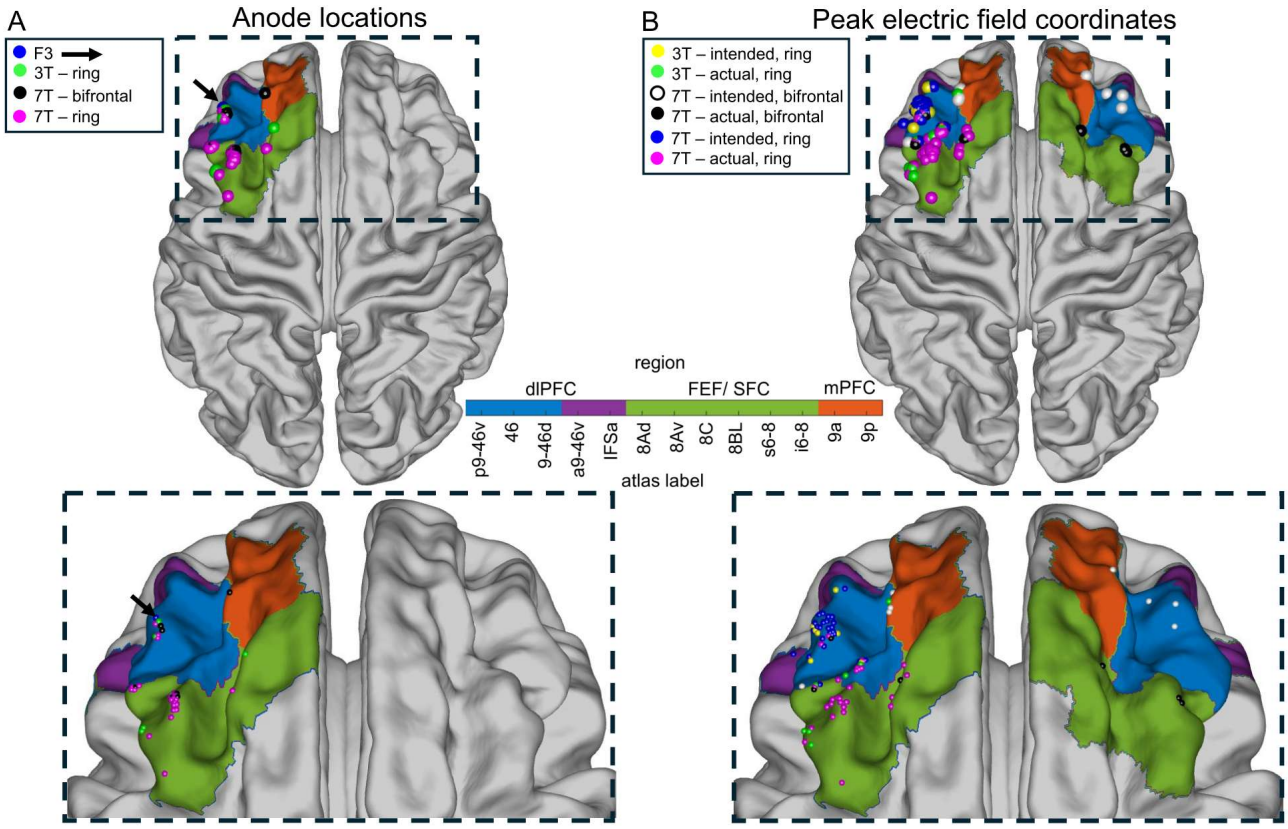


When including all participants, the group-averaged electric field strength was lower for actual electrode positions than for intended positions (Figure 6, upper panel), while the standard deviation was higher (Figures 6, lower panel). This indicates that electrode placement deviations reduced the overall group-averaged electric field strength and increased variability between participants

**Figure 5:** Simulated electric field strength in four participants and two different electrode setups. Values of the 99.9th percentile of the electric field strength are shown in blue, values of the distance between the intended and actual anode location are shown in green and values of the mean electric field magnitude in the dlPFC are shown in purple. A head mesh is shown for each participant with cranial landmarks and intended (pink) as well as actual (blue) electrode positions.

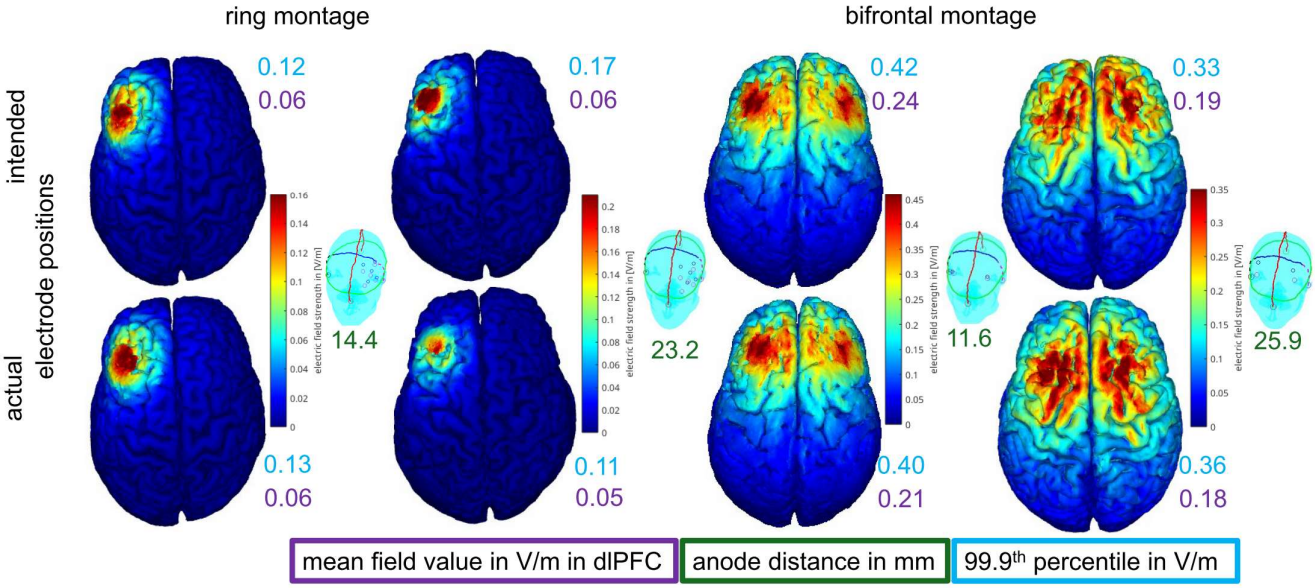


**Figure 6:** Mean and standard deviation of electric field magnitude as well as mean of the normal component of the electric field for all participants (simulated for intended and actual electrode positions).

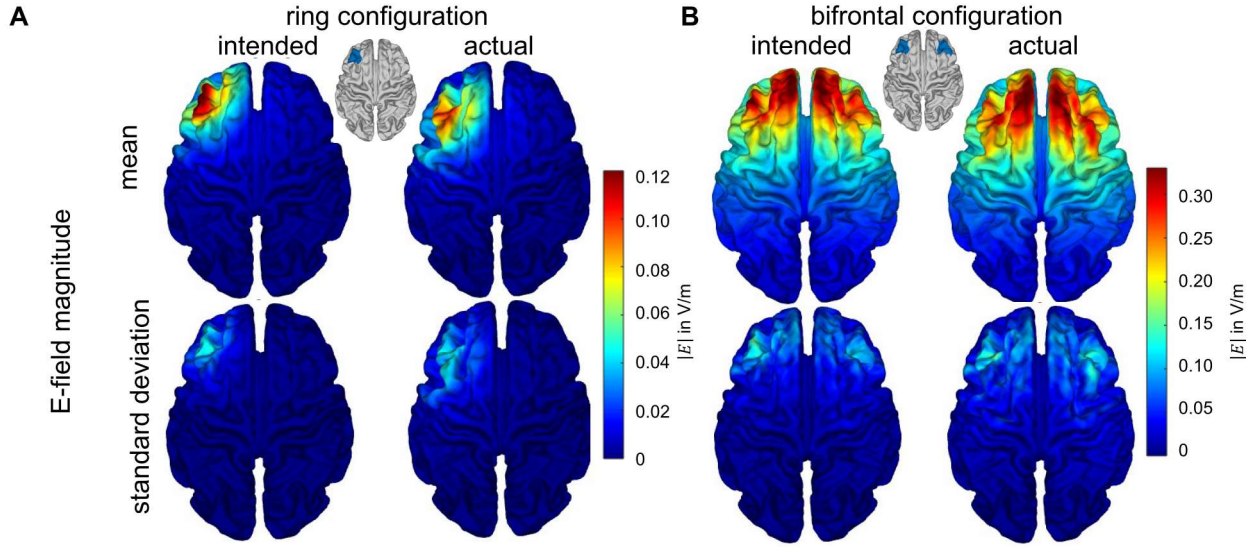


Finally, we compared the mean magnitude E-field values for intended and actual electrode positions (Figure 7) in our target region. We found significant differences (ring-shaped, $p < 0.001$; bifrontal, $p = 0.008$) between the electric field magnitude for actual (ring-shaped median = 0.06 V/m, IQR = 0.03 V/m;

bifrontal median = 0.21 V/m, IQR = 0.10 V/m) compared to intended positions (ring-shaped median = 0.09 V/m, IQR = 0.04 V/m; bifrontal median = 0.23 V/m, IQR = 0.12 V/m) for 7 T data but not for 3 T data. For the E-field magnitude, IQRs were much larger for the bifrontal setup (0.10 – 0.12 V/m) than for the ring-shaped setup (0.02 – 0.04 V/m). This indicates that deviations in electrode placement can meaningfully alter the strength of the electric field in a target region, particularly for data acquired at 7 T.

**Figure 7:** Mean electric field magnitude and normal component of the electric field within the dlPFC for intended and actual electrode positions. Data are grouped by scanner and electrode configuration (3 T, blue; 7 T, bifrontal – orange; 7 T, ring–shaped - yellow).

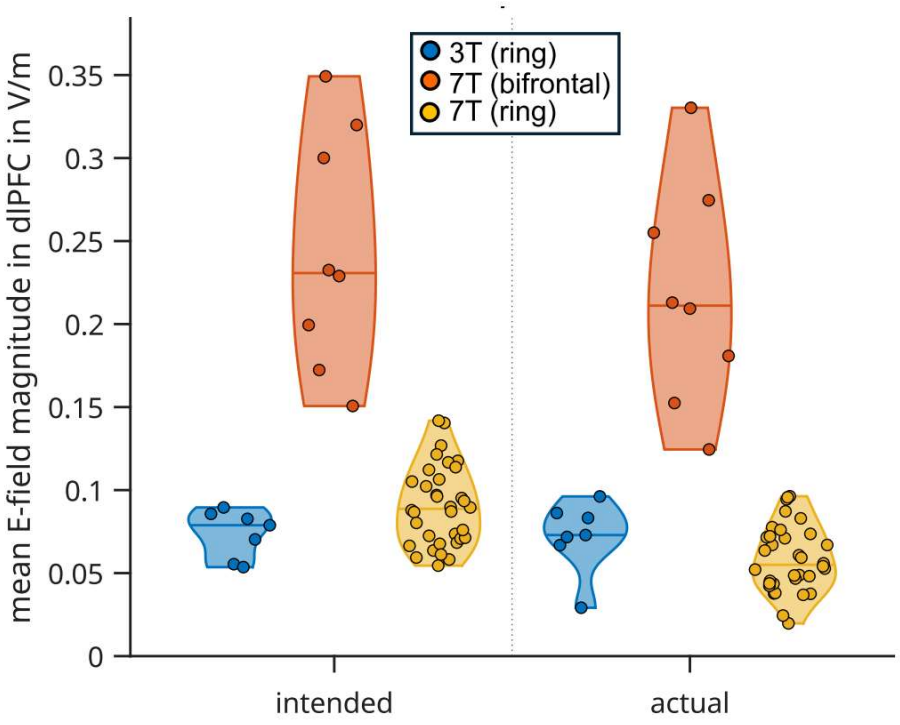


**Discussion**

This study introduces an algorithm that automatedly extracts tDCS electrode coordinates from structural MRI. The algorithm extracts electrode positions with high accuracy and obviates the need to segment electrodes manually[17,18,26]. The algorithm includes seven steps from first segmentation of all electrodes to the final extraction of coordinates. It requires structural MRI data (and electrode holders filled with MR-visible gel), a head mesh, and a tissue segmentation (e.g., by using SimNIBS' CHARM

algorithm). Using the tissue segmentation, it is straightforward to filter actual biological tissues (i.e., the brain, skull, and soft tissue). However, MR images can contain artifacts - for example, from motion - that appear as noisy, high-intensity regions similar to the signal of a gel-filled electrode. To account for that, we incorporate a spatial prior during segmentation that constrains where electrodes can be located (i.e., on the right/left hemisphere or at the front/back of the head). For the same reason, we filter connected components based on size and elongation before extracting electrode coordinates. Conversely, when little gel is used, electrodes may produce only a weak MR signal and can appear faint and disconnected. To accommodate varying signal intensities and degrees of connectedness of electrode 'blobs', the algorithm uses adjustable input parameters – a thresholding factor and a 'smallblobsize' parameter – and the coordinate extraction step is designed to remain robust even when electrode visibility is poor.

The algorithm extracted electrode coordinates very accurately as the distance between algorithm- and reader-derived coordinates was within 1 mm of the distance between readers. There were a few electrodes for which the distance between reader and algorithm was larger. For most of these electrodes the distance between readers was large, too, indicating that larger algorithm-reader differences were related to disagreement between readers. This might be because one of the readers did not find the correct electrode location. In particular for 3 T data, readers reported difficulties finding electrode locations (possibly due to less MR-visible gel). These findings underscore that manual electrode placement is not only time-consuming and prone to reader-dependent bias, but also highlights a broader challenge in tDCS research: verifying electrode positions accurately is difficult, and deviations from intended placement can substantially affect stimulation outcomes. While a deviation of 10-15 mm from intended positions is common when using conventional tDCS[19,20], an electrode placement accuracy < 10 mm for reliable stimulation is recommended[19]. Jog et al.[12] introduced a neuronavigation-based approach that resulted in an average electrode placement error of 7.0 mm, which falls within reliability recommendations. Our proposed algorithm also achieves the level of accuracy required for tDCS studies, with a median localization error of 2.3 mm. Its deviation was within

1 mm of inter-reader variability, confirming human-level accuracy. Hence, the algorithm enables reliable and effortless quantification of electrode placement errors.

Besides accurate and precise electrode placement, anatomical differences between individuals strongly influence the resulting current distribution[35,36]. In accordance with previous studies we found, for example, that only 50 % of the peak electric field coordinates based on intended positions were located within our target region, when using the bifrontal setup. In addition, in our data, the bifrontal setup showed slightly higher variability, as the range of the electric field magnitude was larger than that of the ring setup. This is partly in agreement with previous studies, as one study reported that more diffuse current flow produced by a less focal montage will be aggravated by individual differences[37]. However, in another study, higher focality (e.g., using a ring-shaped setup) led to more variability between participants[38]. In our study, the higher variability within the bifrontal montage indicates that the broader and less focal current flow may be more sensitive to inter-individual anatomical differences. However, the bifrontal setup group was smaller than the ring-shaped setup group. Hence, this needs to be confirmed in larger samples.

Concerning the impact of deviations from intended positions on the resulting electric field, Jog and colleagues reported that 10 mm deviations may lead to a 5-15 % reduction of the electric field[12]. In two example participants with electrode position deviations of approximately 10-15 mm, we found however, that the electric field was reduced by less than 10 %. For larger deviations (> 20 mm), we observed a 35 % reduction in the case of the ring montage which falls within the range of 27-45 % as reported in the literature[12,17]. Hence, electrode placement errors and electric field changes in our data mostly mirrored those previously reported and indicate systematic effects.

Deviations from intended electrode positions alter the electric field but do not predict stimulation efficacy. Such predictions require markers of target engagement, including cerebral blood flow[12,39,40], functional MRI[27,41,42], or MR spectroscopy[43,44]. The algorithm proposed in our study can quantify the deviation between intended and actual electrode positions, which can then be linked to those markers.

This provides a foundation for future studies to relate placement accuracy directly to physiological or behavioural effects.

Our study may have some limitations. First, the spatial priors were established for the specific electrode configurations of the current study. However, they can easily be adjusted to other electrode positions or target regions (e.g., by using additional elseif statements in the function `electrode_loc_prior`). The validity of priors for other electrode montages has to be tested before it can be applied to larger studies. Second, the algorithm relies on the MR-visible gel surrounding the electrodes. It cannot be used for setups that do not use MR-visible gel and it may be harder to find electrodes reliably if the amount of MR-visible gel is low. Third, the two readers were asked to find electrodes but not to assign anodes and cathodes. The automatic assignment of electrodes could be an error source. It seemed, however, infeasible for the readers to find specific electrodes in a timely manner. Fourth, the full automation of this algorithm is limited as it will ask for operator input in case of ambiguous anode locations. However, that only occurred in ~ 10 % of the data and takes only a few seconds.

In conclusion, the developed algorithm automatedly extracts actual electrode positions in studies using in-scanner tDCS. This obviates the need to manually segment electrode positions from structural MRI. The algorithm can be used to quantify deviations between actual and intended electrode positions, which can be linked to established markers of target engagement and, ultimately, to stimulation efficacy.

**Data availability statement**

The code of the proposed algorithm is freely available on github (https://github.com/SinaStraub/tDCS_automated_electrode_location_from_MRI/tree/main). We also provide two datasets (bifrontal and ring-shaped setup) to test the algorithm.

**Funding**

This project has been funded by the Swiss National Science Foundation (grant number 218252 to JP).

**Acknowledgements**

We thank Lea Raas, Aaron Friedli, Salome Flammer, Tamara Bachmann, Theresa Halbritter, Fabian Schmid and Jil Beckmann for their help in recruitment and data acquisition. We thank all participants for their time and support of the study.

**References**


1. Nitsche MA, Paulus W. Excitability changes induced in the human motor cortex by weak transcranial direct current stimulation. *J Physiol*. 2000;527(3):633-639. doi:10.1111/j.1469-7793.2000.t01-1-00633.x
2. Stagg CJ, Nitsche MA. Physiological Basis of Transcranial Direct Current Stimulation. *The Neuroscientist*. 2011;17(1):37-53. doi:10.1177/1073858410386614
3. Woods AJ, Antal A, Bikson M, et al. A technical guide to tDCS, and related non-invasive brain stimulation tools. *Clin Neurophysiol*. 2016;127(2):1031-1048. doi:10.1016/j.clinph.2015.11.012
4. Ruf SP, Fallgatter AJ, Plewnia C. Augmentation of working memory training by transcranial direct current stimulation (tDCS). *Sci Rep*. 2017;7(1):876. doi:10.1038/s41598-017-01055-1
5. Fregni F, Boggio PS, Nitsche M, et al. Anodal transcranial direct current stimulation of prefrontal cortex enhances working memory. *Exp Brain Res*. 2005;166(1):23-30. doi:10.1007/s00221-005-2334-6
6. Nikolin S, Lauf S, Loo CK, Martin D. Effects of High-Definition Transcranial Direct Current Stimulation (HD-tDCS) of the Intraparietal Sulcus and Dorsolateral Prefrontal Cortex on Working Memory and Divided Attention. *Front Integr Neurosci*. 2019;12:64. doi:10.3389/fnint.2018.00064
7. Brunoni AR, Ferrucci R, Fregni F, Boggio PS, Priori A. Transcranial direct current stimulation for the treatment of major depressive disorder: A summary of preclinical, clinical and translational findings. *Prog Neuropsychopharmacol Biol Psychiatry*. 2012;39(1):9-16. doi:10.1016/j.pnpbp.2012.05.016
8. Yachou Y, Bouaziz N, Makdah G, et al. Transcranial direct current stimulation in patients with depression: An electric field modeling meta-analysis. *J Affect Disord*. 2025;374:540-552. doi:10.1016/j.jad.2025.01.001

9. Brunoni AR, Nitsche MA, Bolognini N, et al. Clinical research with transcranial direct current stimulation (tDCS): Challenges and future directions. *Brain Stimulat*. 2012;5(3):175-195. doi:10.1016/j.brs.2011.03.002

10. Lefaucheur JP, Antal A, Ayache SS, et al. Evidence-based guidelines on the therapeutic use of transcranial direct current stimulation (tDCS). *Clin Neurophysiol*. 2017;128(1):56-92. doi:10.1016/j.clinph.2016.10.087

11. Müller D, Habel U, Brodkin ES, Weidler C. High-definition transcranial direct current stimulation (HD-tDCS) for the enhancement of working memory – A systematic review and meta-analysis of healthy adults. *Brain Stimulat*. 2022;15(6):1475-1485. doi:10.1016/j.brs.2022.11.001

12. Jog M, Anderson C, Kim E, et al. A novel technique for accurate electrode placement over cortical targets for transcranial electrical stimulation (tES) clinical trials. *J Neural Eng*. 2021;18(5):056049. doi:10.1088/1741-2552/ac297d

13. Okamoto M, Dan H, Sakamoto K, et al. Three-dimensional probabilistic anatomical cranio-cerebral correlation via the international 10–20 system oriented for transcranial functional brain mapping. *NeuroImage*. 2004;21(1):99-111. doi:10.1016/j.neuroimage.2003.08.026

14. Herwig U, Satrapi P, Schönfeldt-Lecuona C. Using the International 10-20 EEG System for Positioning of Transcranial Magnetic Stimulation. *Brain Topogr*. 2003;16(2):95-99. doi:10.1023/B:BRAT.0000006333.93597.9d

15. Rich TL, Gillick BT. Electrode Placement in Transcranial Direct Current Stimulation—How Reliable Is the Determination of C3/C4? *Brain Sci*. 2019;9(3):69. doi:10.3390/brainsci9030069

16. De Witte S, Klooster D, Dedoncker J, Duprat R, Remue J, Baeken C. Left prefrontal neuronavigated electrode localization in tDCS: 10–20 EEG system versus MRI-guided neuronavigation. *Psychiatry Res Neuroimaging*. 2018;274:1-6. doi:10.1016/j.pscychresns.2018.02.001

17. Niemann F, Riemann S, Hubert AK, et al. Electrode positioning errors reduce current dose for focal tDCS set-ups: Evidence from individualized electric field mapping. *Clin Neurophysiol*. 2024;162:201-209. doi:10.1016/j.clinph.2024.03.031

18. Indahlastari A, Dunn AL, Pedersen S, et al. The importance of accurately representing electrode position in transcranial direct current stimulation computational models. *Brain Stimulat*. 2023;16(3):930-932. doi:10.1016/j.brs.2023.05.010

19. Opitz A, Yeagle E, Thielscher A, Schroeder C, Mehta AD, Milham MP. On the importance of precise electrode placement for targeted transcranial electric stimulation. *NeuroImage*. 2018;181:560-567. doi:10.1016/j.neuroimage.2018.07.027

20. Woods AJ, Bryant V, Sacchetti D, Gervits F, Hamilton R. Effects of Electrode Drift in Transcranial Direct Current Stimulation. *Brain Stimulat*. 2015;8(3):515-519. doi:10.1016/j.brs.2014.12.007

21. Horvath JC, Forte JD, Carter O. Quantitative Review Finds No Evidence of Cognitive Effects in Healthy Populations From Single-session Transcranial Direct Current Stimulation (tDCS). *Brain Stimulat*. 2015;8(3):535-550. doi:10.1016/j.brs.2015.01.400

22. Indahlastari A, Albizu A, Nissim NR, Traeger KR, O'Shea A, Woods AJ. Methods to monitor accurate and consistent electrode placements in conventional transcranial electrical stimulation. *Brain Stimulat*. 2019;12(2):267-274. doi:10.1016/j.brs.2018.10.016

23. Saturnino GB, Puonti O, Nielsen JD, Antonenko D, Madsen KH, Thielscher A. SimNIBS 2.1: A Comprehensive Pipeline for Individualized Electric Field Modelling for Transcranial Brain Stimulation. In: Makarov S, Horner M, Noetscher G, eds. *Brain and Human Body Modeling*. Springer International Publishing; 2019:3-25. doi:10.1007/978-3-030-21293-3_1

24. Huang Y, Datta A, Bikson M, Parra LC. Realistic volumetric-approach to simulate transcranial electric stimulation—ROAST—a fully automated open-source pipeline. *J Neural Eng*. 2019;16(5):056006. doi:10.1088/1741-2552/ab208d

25. Grignard M, Geuzaine C, Phillips C. Shamo: A Tool for Electromagnetic Modeling, Simulation and Sensitivity Analysis of the Head. *Neuroinformatics*. 2022;20(3):811-824. doi:10.1007/s12021-022-09574-7

26. Indahlastari A, Albizu A, Kraft JN, et al. Individualized tDCS modeling predicts functional connectivity changes within the working memory network in older adults. *Brain Stimulat*. 2021;14(5):1205-1215. doi:10.1016/j.brs.2021.08.003

27. Li H, Shi H, Jiang S, et al. Effects of antagonistic network-targeted tDCS on brain co-activation patterns depends on the networks' electric field: a simultaneous tDCS-fMRI study. *NeuroImage*. 2025;316:121318. doi:10.1016/j.neuroimage.2025.121318

28. Puonti O, Van Leemput K, Saturnino GB, Siebner HR, Madsen KH, Thielscher A. Accurate and robust whole-head segmentation from magnetic resonance images for individualized head modeling. *NeuroImage*. 2020;219:117044. doi:10.1016/j.neuroimage.2020.117044

29. Thielscher A, Antunes A, Saturnino GB. Field modeling for transcranial magnetic stimulation: A useful tool to understand the physiological effects of TMS? In: *2015 37th Annual International Conference of the IEEE Engineering in Medicine and Biology Society (EMBC)*. IEEE; 2015:222-225. doi:10.1109/EMBC.2015.7318340

30. Jurcak V, Tsuzuki D, Dan I. 10/20, 10/10, and 10/5 systems revisited: Their validity as relative head-surface-based positioning systems. *NeuroImage*. 2007;34(4):1600-1611. doi:10.1016/j.neuroimage.2006.09.024

31. Lloyd S. Least squares quantization in PCM. *IEEE Trans Inf Theory*. 1982;28(2):129-137. doi:10.1109/TIT.1982.1056489

32. Wong MH. grpandplot: An open-source MATLAB tool for drawing box plot and violin plot with automatic multi-way data grouping. Published online November 5, 2022. doi:10.5281/ZENODO.7295877

33. Glasser MF, Coalson TS, Robinson EC, et al. A multi-modal parcellation of human cerebral cortex. *Nature*. 2016;536(7615):171-178. doi:10.1038/nature18933

34. Petre B, Ceko M, Friedman NP, et al. 2016 Glasser MMP1.0 Cortical Atlases. Published online 2023:534271010 Bytes. doi:10.6084/M9.FIGSHARE.24431146.V8

35. Li LM, Uehara K, Hanakawa T. The contribution of interindividual factors to variability of response in transcranial direct current stimulation studies. *Front Cell Neurosci*. 2015;9. doi:10.3389/fncel.2015.00181

36. Antonenko D, Grittner U, Saturnino G, Nierhaus T, Thielscher A, Flöel A. Inter-individual and age-dependent variability in simulated electric fields induced by conventional transcranial electrical stimulation. *NeuroImage*. 2021;224:117413. doi:10.1016/j.neuroimage.2020.117413

37. Datta A, Truong D, Minhas P, Parra LC, Bikson M. Inter-Individual Variation during Transcranial Direct Current Stimulation and Normalization of Dose Using MRI-Derived Computational Models. *Front Psychiatry*. 2012;3. doi:10.3389/fpsyt.2012.00091

38. Mikkonen M, Laakso I, Tanaka S, Hirata A. Cost of focality in TDCS: Interindividual variability in electric fields. *Brain Stimulat*. 2020;13(1):117-124. doi:10.1016/j.brs.2019.09.017

39. Zheng X, Alsop DC, Schlaug G. Effects of transcranial direct current stimulation (tDCS) on human regional cerebral blood flow. *NeuroImage*. 2011;58(1):26-33. doi:10.1016/j.neuroimage.2011.06.018

40. Baeken C, Remue J, Vanderhasselt MA, et al. Increased left prefrontal brain perfusion after MRI compatible tDCS attenuates momentary ruminative self-referential thoughts. *Brain Stimulat*. 2017;10(6):1088-1095. doi:10.1016/j.brs.2017.09.005

41. Jog M, Jann K, Yan L, et al. Concurrent Imaging of Markers of Current Flow and Neurophysiological Changes During tDCS. *Front Neurosci*. 2020;14:374. doi:10.3389/fnins.2020.00374

42. Antonenko D, Thielscher A, Saturnino GB, et al. Towards precise brain stimulation: Is electric field simulation related to neuromodulation? *Brain Stimulat*. 2019;12(5):1159-1168. doi:10.1016/j.brs.2019.03.072

43. Kim S, Stephenson MC, Morris PG, Jackson SR. tDCS-induced alterations in GABA concentration within primary motor cortex predict motor learning and motor memory: A 7T magnetic resonance spectroscopy study. *NeuroImage*. 2014;99:237-243. doi:10.1016/j.neuroimage.2014.05.070

44. Nandi T, Puonti O, Clarke WT, et al. tDCS induced GABA change is associated with the simulated electric field in M1, an effect mediated by grey matter volume in the MRS voxel. *Brain Stimulat*. 2022;15(5):1153-1162. doi:10.1016/j.brs.2022.07.049